

Full Device Evaluation of Metal Halide Perovskite Solar Cells in Low Earth Orbit Aboard the International Space Station

Samuel S. Erickson, Jorge Arteaga, Kaitlyn T. VanSant, Ahmad R. Kirmani, Steven P. Harvey, Joseph M. Luther, Timothy J. Peshek, Lyndsey McMillon-Brown,* and Sayantani Ghosh*

This study investigates how sustained low Earth orbit (LEO) exposure affects metal halide perovskite (MHP) thin films and perovskite solar cells (PSCs). It examines samples deployed on the Materials International Space Station Experiment (MISSE) 15 and 16 missions. Five methylammonium lead iodide (MAPI) thin films are deployed on MISSE-16, each with distinct UV filters to selectively attenuate AM0 spectral bands. While post-flight optical analysis reveals that the least UV-exposed film exhibits the highest emission and lowest non-radiative recombination rate, no clear correlation is observed among the rest, and all MAPI films maintained excellent integrity throughout the mission. MISSE-15 deployed eight PSCs with diverse structures, MHP compositions, and contact materials. Post-flight analysis reveals stable, highly emissive MHPs, but damaged contacts due to ion migration, which caused loss of electrical response. The MISSE missions demonstrate MHPs' suitability for space applications, while highlighting the need for improved interfacial layers and contact materials to enhance charge carrier mobility, prevent ion migration, and improve charge carrier extraction efficiency.

properties that make them suitable for use in space, with studies indicating their durability and potential for high-performance efficiency in low Earth orbit (LEO) conditions.^[2–13] However, perovskite solar cells (PSCs) have been studied extensively for the demands of terrestrial commercialization; the same is not true of PSCs for aerospace applications.^[14] In our previous study, we found that an encapsulated thin film of methylammonium lead iodide (MAPI) exhibited long-term photo-stability, resistance to radiation, and optimal spectral characteristics after a 10-month flight at LEO as part of the 13th Materials for International Space Station Experiment (MISSE-13).^[15–17] This study's results highlight the enormous potential of MHP absorbers to retain their exceptional optoelectronic properties for a prolonged period under LEO conditions. The critical next steps toward

1. Introduction

Power generation will play an increasingly crucial role in sustaining space exploration missions across the solar system and beyond.^[1] Metal halide perovskite (MHP) compounds have

operationalizing MHP-based applications in this environment include the development of resilient device stacks, which include interfacial layers, charge-selective contacts, and encapsulation materials enabling the promise of high specific power of PSCs for the duration of prolonged LEO missions.

In this work, we summarize the results of two separate MISSE missions, each focusing on a different aspect of MHP resilience, both on Earth and in LEO conditions. The first set of data is from MISSE-16 and consists of optical characterization of five blade-coated methylammonium lead iodide (MAPI) films^[18] with UV filters as top layers. The filters had cut-on wavelengths between 220 and 390 nm, which allowed the films to be exposed to specific ranges of the UV region of AM0 radiation, with the end goal of testing MAPI stability to UV exposure. The second set of data is from eight photovoltaic (PV) device stacks aboard the MISSE-15 mission, comprised of different perovskite compositions, including MAPI, mixed cation, and mixed halide MHPs, as well as varying metallic contacts (silver and aluminum). Optical measurements of the samples from both MISSE flights demonstrated that, beyond minor variations, the hybrid organic-inorganic MHP materials remained emissive and intact across the board, confirming their suitability for space-based applications.

S. S. Erickson, J. Arteaga, S. Ghosh
Department of Physics
University of California
Merced, CA 95343, USA
E-mail: sghosh@ucmerced.edu

K. T. VanSant, S. P. Harvey, J. M. Luther
National Renewable Energy Laboratory
Golden, CO 80401, USA

A. R. Kirmani
School of Chemistry and Materials Science
Rochester Institute of Technology
Rochester, NY 14623, USA

T. J. Peshek, L. McMillon-Brown
Photovoltaic and Electrochemical Systems Branch
NASA Glenn Research Center
Cleveland, OH 44135, USA
E-mail: lyndsey.mcmillon-brown@nasa.gov

 The ORCID identification number(s) for the author(s) of this article can be found under <https://doi.org/10.1002/sml.202508232>

DOI: 10.1002/sml.202508232

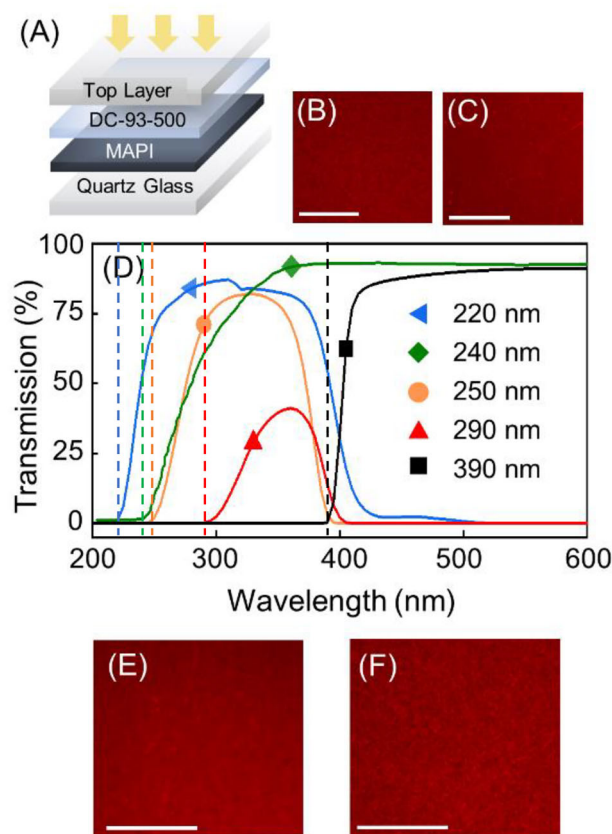


Figure 1. A) Schematic of a stack representative of all MISSE-16 samples. Bold arrows indicate the direction of illumination on the ISS. Confocal images of (B) control and (C) flight sample with borosilicate glass as the top layer. D) Transmission curves of the top layers of all MISSE-16 samples. The threshold wavelengths λ_T used to label data are indicated by dashed lines. $\lambda_T = 240$ nm corresponds to the borosilicate top layer. Confocal images of (E) control and (F) flight sample with a filter of $\lambda_T = 290$ nm as the top layer. Scale bars in confocal images: 100 μm .

2. MISSE-16: UV Tolerance of MAPI in LEO

2.1. MISSE-16 Samples

The schematic in **Figure 1A** is representative of samples used for AM0 UV tolerance testing on MISSE-16. The MAPI film was deposited by blade coating,^[18] followed by annealing and encapsulation using space-qualified Thixotropic Dow Corning (DC) 93–500 silicone elastomer. The top layers varied for the samples, between different UV filters and borosilicate glass. Of the seven samples fabricated, five traveled to Alpha Space Test and Research Alliance, LLC (now Aegis Aerospace) in Houston, TX for environmental testing, including a high vacuum bakeout at 60 °C for 25 hr and 3-axis vibration at 4.5 G_{rms} (where 1 $G_{\text{rms}} = 9.8 \text{ m s}^{-2}$). They were then loaded onto a SpaceX Falcon 9 rocket and launched on the 25th Commercial Resupply Service mission (CRS-25) on July 15, 2022. Aboard the ISS, the samples were deployed on the MISSE-Flight Facility platform in zenith (sun-facing) orientation between August 2022 and February 2023. The MISSE-16 mission concluded with the landing of SpaceX CRS-27 on April 15, 2023, upon which the five samples were returned

to NASA Glenn one month later. Post-flight characterization of all samples began in July 2023, 1.5 years after fabrication.

The control samples used for comparison were fabricated in parallel with the MISSE-16 flight samples, using identical deposition and encapsulation procedures. These controls were stored in a nitrogen ambient glove box for the duration of the MISSE-16 mission. The control samples underwent characterization at the same time as the post-flight samples, ≈ 1.5 years after fabrication. As such, the reported PL lifetimes and intensities reflect the aged state of the MAPI films under realistic storage conditions, not freshly prepared material.

2.2. Confocal and Spectroscopic Characterization

Figure 1B,C are confocal images of the control and flight samples with borosilicate glass^[14] as the top layer; the emission wavelength range is represented as red, while the non-emissive areas appear black. Figure 1D plots the transmission spectra of this top layer along with all the other UV filters used. The wavelengths where the filters start transmitting are denoted by dashed lines and designated threshold wavelengths λ_T . The curve for borosilicate glass has $\lambda_T = 240 \text{ nm}$. Figure 1E,F are confocal images of control and flight samples with $\lambda_T = 290 \text{ nm}$ filter as the top layer. Both flight samples (Figure 1C,F) appear uniform under confocal microscopy, with very few non-emissive regions, and are practically indistinguishable from their respective controls.

To properly record the spectral behavior of the MISSE-16 samples, high-resolution PL maps were taken of each sample over an area of 1 mm^2 for both spectral and time-resolved analysis. The recombination lifetime and PL intensity obtained from these maps are shown in **Figure 2A,B** as box plots. The most noticeable result is that the sample with $\lambda_T = 390 \text{ nm}$ as the top layer has the highest emission intensity and the longest lifetime, and these parameters exceed the averages obtained from the control samples (dashed lines and shading). It is the only sample that is completely shielded from UV radiation and has the lowest emission energy (Figure S1, Supporting Information). A point to note here is that while the observed PL lifetimes are atypical, these align with prior works that report similarly short lifetimes in MAPI films^[19], which can potentially yield excellent power conversion efficiency (PCE). This supports the idea that short PL lifetimes do not necessarily constrain V_{OC} .^[20,21] For an indication of what the V_{OC} and PCE of these MISSE-16 MAPI films could be, MISSE-15 data reported in Section 3.2 describes MAPI solar cells (Figure 4–c) that were fabricated using identical protocols for the MAPI film deposition that also demonstrate similar recombination lifetimes (Figure 5).

The behavior of the other samples cannot be correlated easily with the filter transmission bands, but they do demonstrate a trend upon light soaking, shown in Figure 2C. MISSE-16 samples were subjected to 5 h of UV light exposure to determine photostability and were illuminated through the top layer with a 360 nm UV lamp. Spectrally resolved PL was captured every 10 s for 5 h to track changes in the spectral properties, and the PL intensity is plotted in Figure 2C as a function of photo exposure time. The counts are normalized to their initial intensities to remove the effect of sample disparities and highlight the trends. The $\lambda_T = 390 \text{ nm}$ sample, which had the highest PL emission and

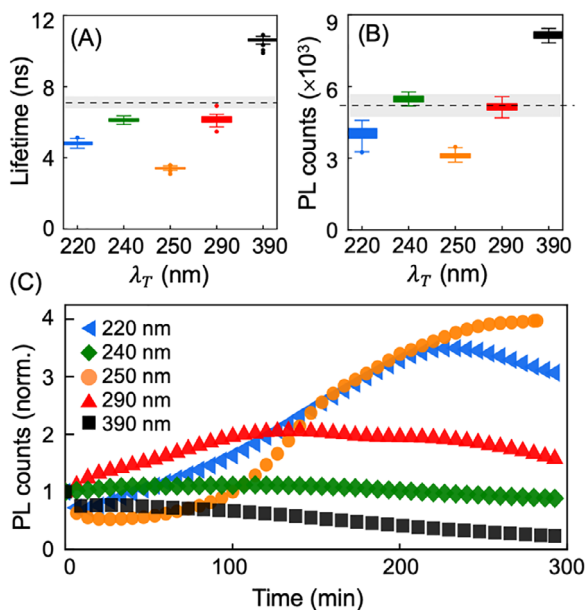


Figure 2. Boxplots for all MISSE-16 samples summarizing (A) recombination lifetime, and B) PL intensity. Each box is composed of 25 data points taken in a 1 mm² grid across each sample. The shaded regions indicate the spread observed in the control samples with different filters, and the dashed lines represent the controls' averages. C) Spectrally integrated PL intensity of all MISSE-16 samples recorded every 10 s for 5 h of continuous 360 nm illumination. Curves are labelled by λ_T and PL emission normalized to the initial value.

lifetime, steadily darkens, but that is not photo-driven, as the top layer has no transmission at the excitation wavelength. The $\lambda_T = 240$ and $\lambda_T = 290$ nm samples, which are nearly at par with the controls, are relatively stable, though the latter does show some initial brightening.

To distinguish between UV-driven effects and general light-induced relaxation, we compared the PL evolution of the MISSE-16 sample with a 390 nm UV filter (black squares in Figure 2C) to a freshly-prepared sample fabricated under identical conditions and measured immediately after fabrication, but also covered with borosilicate glass. Despite both being UV-shielded, the fresh control exhibited a slow increase in PL intensity under continuous 360 nm illumination, while the aged MISSE-16 sample showed a gradual decline. This contrast suggests that while some slow recovery processes can occur even without UV (e.g., thermal or carrier-assisted relaxation), they are strongly dependent on the initial material quality and storage history. The absence of brightening in the aged MISSE-16 390 nm sample, combined with the clear brightening in the UV-exposed samples (220 and 250 nm), confirms that rapid PL recovery is predominantly driven by direct UV interaction, not ambient light exposure or spontaneous annealing. These supporting results are included as Figure S2 (Supporting Information).

Exposing MHPs to UV light can indeed lead to both photodarkening and photo-brightening effects, depending on various factors. This dual behavior highlights the complex photophysics of these materials. UV exposure can degrade MHPs by forming defects, accelerating ion migration, and causing structural decomposition, potentially reducing PL intensity.^[22–24] Alternately, UV

radiation can also facilitate halide migration to passivate defects, particularly at surfaces and grain boundaries, or induce slight structural changes in the perovskite lattice, both of which could lead to enhanced optical properties.^[25–28] The two samples that brighten between 3- and 4-fold ($\lambda_T = 220$ and 250 nm) are the ones with lowest emission intensity and shortest lifetimes and are therefore likely to have a high concentration of defects acting as non-radiative recombination centers. The observation that these initially poor-performing films show the greatest improvement under UV light soaking suggests that the UV treatment is effectively addressing the primary factors limiting their emission intensity and recombination lifetimes.

Overall, the results of optical characterization and light-soaking of MISSE-16 samples indicate that UV radiation does impact MAPI spectral behavior, since the $\lambda_T = 390$ nm film has the highest PL counts and lifetimes. However, the other samples are minimally affected and show significant recovery upon prolonged photo exposure. The conclusion is therefore that MAPI is strongly resistant to UV damage, even at the elevated intensities of AM0 radiation. The UV stability observed in MISSE-16 samples, particularly the PL enhancement in those exposed to short-wavelength UV, highlights that MAPI degradation is strongly context-dependent. In the absence of oxygen and moisture, as in spaceflight or in well-encapsulated systems, UV exposure can activate beneficial healing processes, in contrast to degradation pathways reported under ambient laboratory conditions.

3. MISSE-15: MHP Devices in LEO

3.1. Sample Architectures of Perovskite Solar Cells on MISSE-15

Having explored the effect of LEO stressors on isolated MHP films, we turn to full perovskite solar cells (PSCs). Aboard the MISSE-15 mission, we flew PSCs in zenith (sun-facing) orientation for eight months. Figure 3 shows schematics of three different architectures, and the samples on board included two of each kind. Half the cells were of *n-i-p* structure, with the electron transport layer deposited before the MHP absorber, while the other half were *p-i-n*. The *p-i-n* devices included two cells with a MAPI (CH₃NH₃PbI₃) absorber layer (Figure 3A) and two with a formamidinium (FA)-rich triple cation (Cs_{0.04}MA_{0.05}FA_{0.91}Pb(I_{0.95}Br_{0.05})₃) absorber layer (Figure 3C, F-3cat). Additional device fabrication details can be found in the experimental methods section. The *n-i-p* devices included two cells with a triple cation absorber layer (Cs_{0.05}(MA_{0.17}FA_{0.83})_{0.95}Pb(I_{0.83}Br_{0.17})₃, Figure 3B, (3cat)).^[29] The most significant difference between these samples was the use of silver (Ag) in the *p-i-n* devices and aluminum (Al) in the *n-i-p* cells as electrical contacts, along with variations in the charge transport layers. In addition to the above, two all-inorganic *n-i-p* cells (CsPbI₂Br) with Al contacts were also included (Figure S3, Supporting Information). All architectures had corresponding control samples that remained on Earth. The flight and control samples were fabricated in February and March 2021. All flight and control samples were encapsulated with DC 93–500 silicone elastomer and cover glass. Control samples were held in a nitrogen ambient glovebox environment for the duration of the mission. Flight samples were shipped from NREL to Aegis Aerospace (in Houston) on March 11, 2021, where they were integrated into

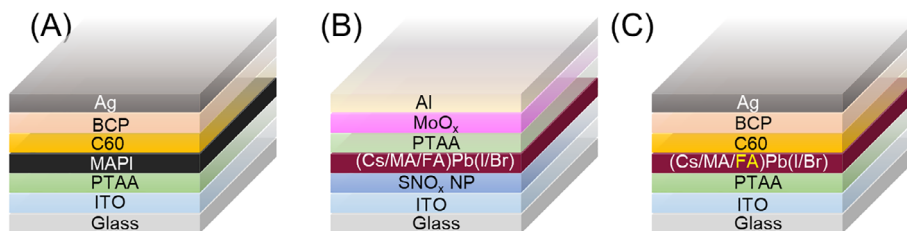


Figure 3. Schematics of device architectures for MISSE-15, including A) p-i-n MAPI₃ cell, B) n-i-p triple cation (3cat) cell, and C) p-i-n formamidinium-rich triple cation (F-3cat) cell. Two devices of each architecture were flown aboard the ISS.

the MISSE carrier cases and kept in a cleanroom environment until they were shipped to Florida for launch. The MISSE samples were loaded onto a SpaceX Falcon 9 rocket and launched on the 23rd Commercial Resupply Service mission (CRS-23) on August 29, 2021. Aboard the ISS, the samples were deployed on the MISSE-Flight Facility platform in zenith (sun-facing) orientation between November 20, 2021, and July 31, 2022. The samples were electrically coupled to the platform with a conductive carrier sheet to prevent electrostatic discharge to the ISS. The MISSE-15 mission concluded with the landing of SpaceX CRS-25 on August 20, 2022. The flight samples were returned to NREL on September 29, 2022. Post-flight characterization of all samples began on October 12, 2022, 1.5 years after fabrication.

3.2. Preliminary Characterization

Figure 4 shows pre- and post-flight images of MAPI and 3cat PSCs along with their current–voltage (I - V) characteristics. Both Ag (Figure 4A) and Al (Figure 4D) contacts appear uniform and reflective in images taken pre-flight. Figure 4B,E are images of the same samples taken upon their return from an eight-month

stint on the ISS, and the contacts show clear signs of degradation. However, while the Ag contact pads of the MAPI and F-3cat (Figure S4, Supporting Information) samples turned from grey and reflective to yellow and dull starting at the edges, the Al of the 3cat and inorganic cells exhibit smaller, scattered patches of yellow defects across nearly all contact pads. Figure 4C,F provides current–voltage (J - V) curves of the MAPI and 3cat PSCs, respectively, for the highest performing pixel on each of the samples. Post-flight, neither sample yields current at any tested voltage. This is true of all MISSE-15 samples, indicative of electrical failure and possible delamination of contacts from the device. Despite the electrical failure of these devices, our optical characterization reveals considerable information \approx 1.5 years of exposure to both Earth and LEO conditions on these PSCs, except for the inorganic devices, which were completely degraded, appearing transparent and non-emissive (Figure S4, Supporting Information).

3.3. Spectral and Time-Resolved Characterization

To record the optical properties of the MISSE-15 samples, multiple high-resolution PL maps were taken across each sample in

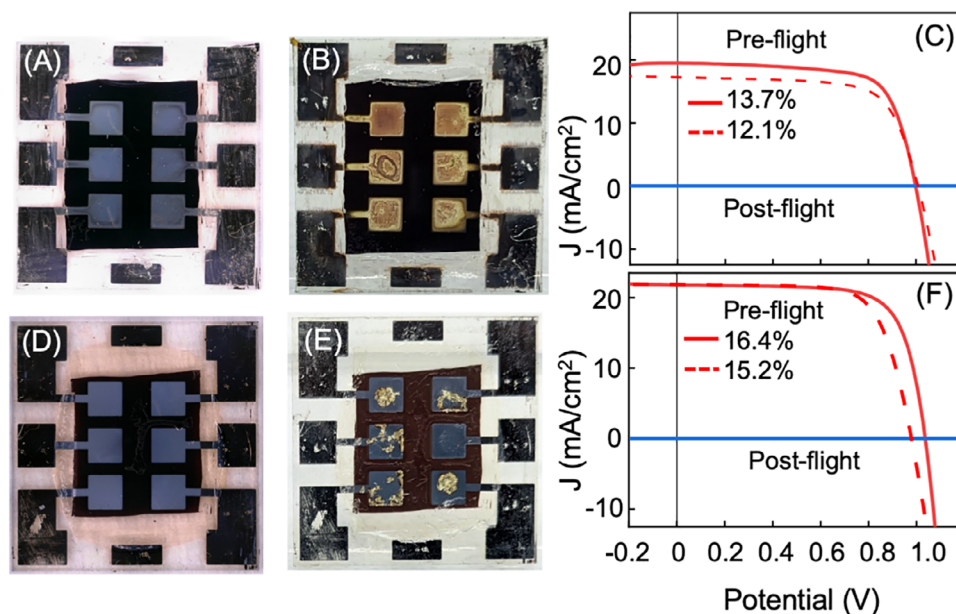


Figure 4. Optical images of MAPI samples with Ag contacts (A) pre- and (B) post-flight. C) Current–voltage response of the same. Images of 3cat cell with Al contacts (D) pre and (E) post flight, and F) Current–voltage response. For pre-flight data, solid (dashed) lines indicate measurements in forward (reverse) bias. All MISSE-15 samples were electrically non-responsive post-flight.

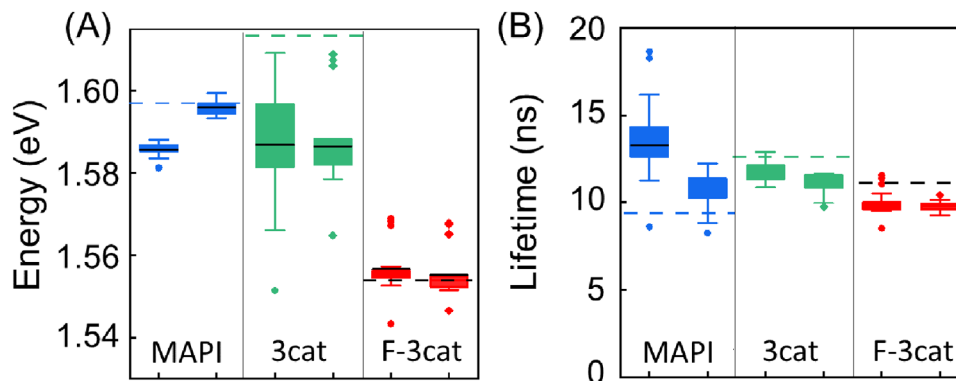


Figure 5. A) Emission energy, and B) recombination lifetimes of flight samples. For each MHP composition, data is collected from spatially resolved PL maps of both devices of each kind. Dashed lines are average values derived from maps of equivalent controls.

a 1.8×2 mm grid from a region between the electrical contact pads. The PL emission is analyzed both spectrally and temporally, and emission energy and recombination lifetimes obtained from these measurements are plotted in **Figure 5**. Overall, the three types of flight samples behave similarly to their respective controls and show few signs of degradation. F-3cat flight samples returned to Earth with almost no change in their emission energy compared to their controls in **Figure 5A**, while the maximum average energy difference between flight and control samples is seen among 3cat cells. On average, these devices emit 27 meV lower in energy than their control, a gap like the difference observed between the MISSE-13 pre- and post-flight MAPI films.^[15] The greatest FWHM increase (**Figure S5**, Supporting Information) is also found between the 3cat flight and control samples, though only by 5.8 meV, which is minimal compared to the spectral FWHM value ≈ 90 meV. The FWHM of the MAPI and F-3cat differs from their controls on average by 1–3 meV. The charge recombination lifetimes plotted in **Figure 5B** show close agreement between flight and control devices.

3.4. MAPI and F-3cat PSCs with Ag Contacts

To better understand how the MHP layer was affected by contact degradation, PL maps were taken both between (3) and within (1 & 2) the active area of the pixels for the MAPI flight sample. **Figure 6A** is an optical image of the sample taken post-flight, where we have numbered two contacts (1 and 2) and a region between contacts (3) to indicate where PL data were collected from. **Figure 6B,C** are fluorescence confocal images of MAPI control and flight samples, respectively, mapping regions between the contacts. Image of the flight sample confirms that despite damage to the electrical contacts, the MAPI film remains emissive, at least between pixels. For spectrally resolved data of the MAPI region behind the contacts, we chose “1” and “2” because they appeared the most and least degraded of the six, respectively. The differences in MAPI spectral properties from these two regions and “3” are summarized in **Figure 6D,E**, with data derived from spatially-resolved maps. The PL emission intensity in **Figure 6D** from contact 1 is highest on average, varying by a factor of eight across the region mapped. Compared to the intensity from the region between contacts (“3”), this is highly non-uniform and

is likely due to scattering from the eroded and yellowed metallic pad. The MAPI behind the least degraded contact (“2”) is darker but less variable. The lower emission counts result from the metal layer being intact and reducing transmission of both excitation and PL.

The biggest difference between on and off pixels is in the emission energy, shown in **Figure 6E**, where the MAPI film behind the contacts (1 and 2) emits nearly 20 meV higher than MAPI in region 3. Blue shift of PL emission was observed in the case of the MISSE-13 MAPI films, where it was attributed to strain resulting from repeated thermal cycling in LEO.^[15] In this case, the specific spatial variation in the emission energy suggests either localized strain or, more likely, chemical degradation related to the contact deterioration. Ag is prone to oxidation and migration, especially when exposed to air, moisture, or elevated temperatures, which can lead to device degradation and reduced performance over time.^[30–32] For MHPs with the C60/BCP/Ag structure, Ag diffuses into the perovskite layer, creating defects and trap states, and reacts with the halide ions, forming silver halide compounds at the contacts. Additionally, several factors in the LEO environment may contribute to an increased ion migration, including rapid thermal cycling, high-energy radiation, ultrahigh vacuum, etc. However, it should be noted that migration of halides to the Ag contact layer of solar cells with the C60/BCP/Ag structure has been observed in both flight cells and control samples held in a nitrogen glovebox environment (**Figure S6**, Supporting Information). The variation in recombination lifetimes between the three regions (**Figure S7A**, Supporting Information) is commensurate with the observation in **Figure 6E**, with a greater blue-shift accompanied by shorter lifetimes. The range of average linewidths is nearly insignificant, less than 3 meV across all areas (**Figure S7B**, Supporting Information). Altogether, these results lead to the conclusion that the MHP layer behind metal contacts is degraded, and this degradation is not uniform across all pixels of a device.

Figure 7A shows an F-3cat flight sample with Ag-contacts. The metal pads show yellow discoloration predominantly along the edges. An edge of the bottom left contact pad is magnified with a transmission optical microscope in **Figure 7B**. The intact metal blocks light from below as expected, but the degraded region appears overwhelmingly yellow, obfuscating any sign of emission through the degraded Ag. The MHP underneath these yellow

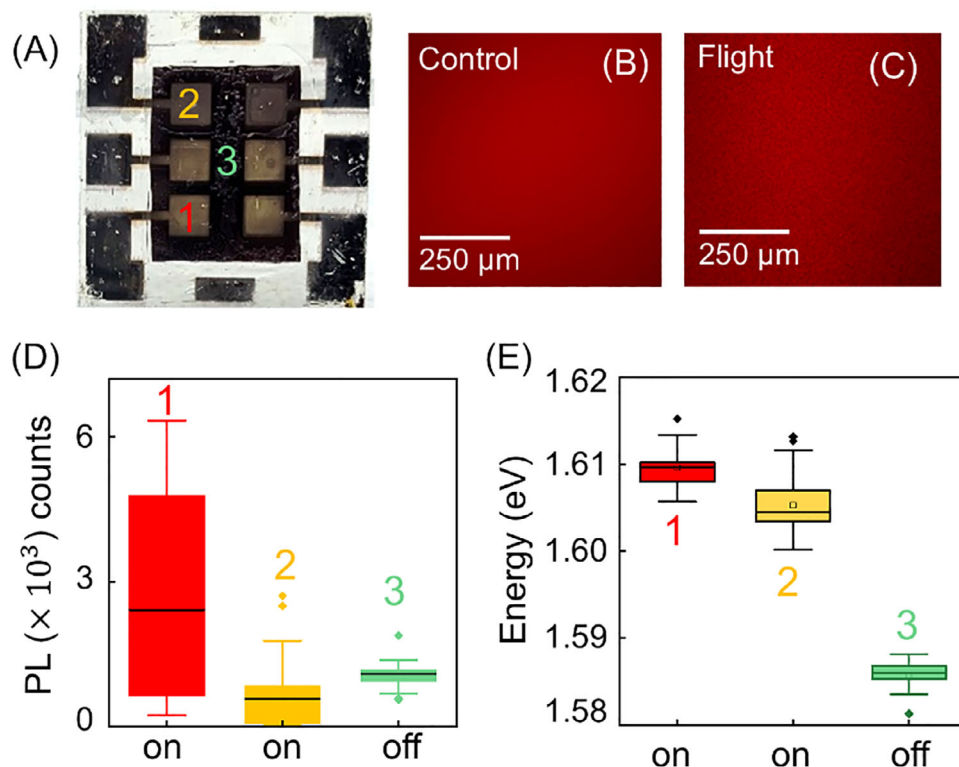


Figure 6. A) Front image of MAPI sample (with Ag contact) taken post-flight. Confocal images of MAPI B) control and C) flight samples, between the contact pads. D) Emission intensity, and E) emission energy for the three areas indicated in (A). Areas 1 and 2 are areas on the contacts, while area 3 is off the contact area.

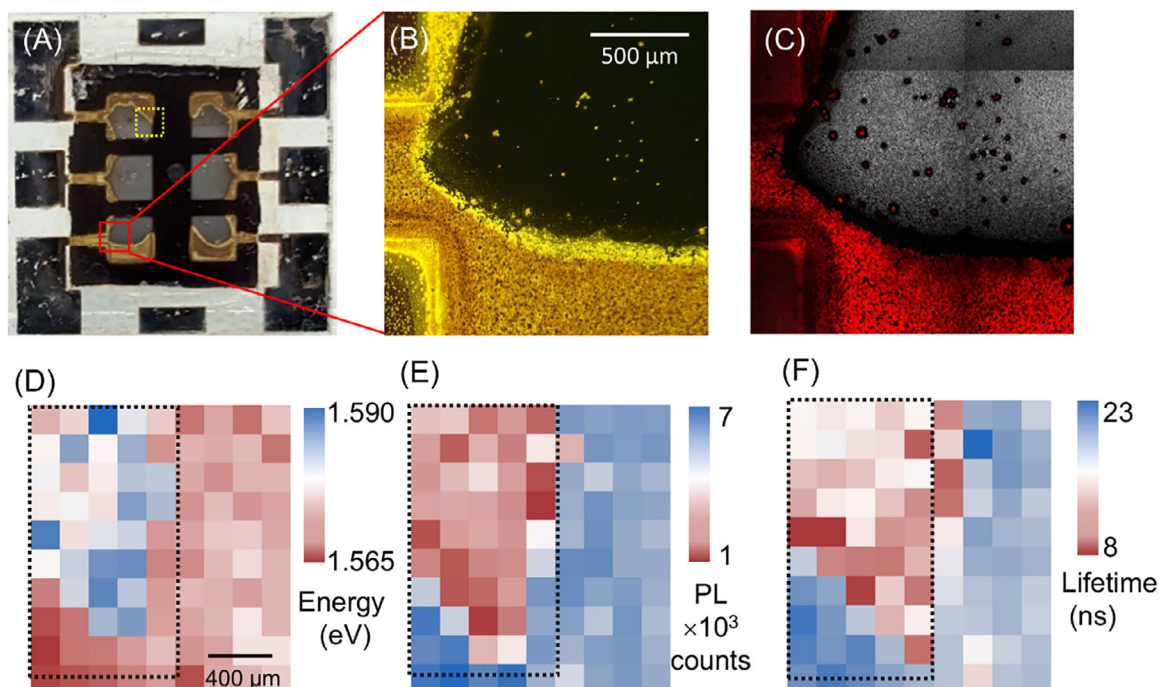


Figure 7. A) Optical image of F-3cat cell with Ag contacts taken post-flight. B) Transmission optical microscope and C) combined reflection (gray) and PL (red) confocal image of the same region indicated in (A). Heatmaps of D) PL emission energy, E) PL intensity, and F) charge recombination lifetime of the region indicated in (A) by the dashed yellow square. The dashed enclosure in (D–F) roughly outlines the area on the contact pad.

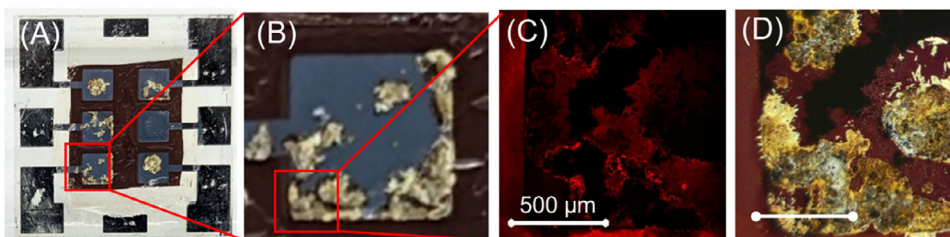


Figure 8. A) Front image of the 3cat flight sample. B) Magnified image of the bottom-left Al contact. C) 4x magnification confocal fluorescence image of this region. D) 4x magnification transmission optical microscope image. The characteristic dark red of the MHP layer matches one-to-one with the fluorescent regions in (C).

regions, however, is emissive as seen in Figure 7C. The large red regions match well with the yellow of Figure 7B, as do the small specks of yellow and red across the Ag pad. Additional quantitative spectral data are derived from spatially-resolved PL maps of the region denoted by the yellow dashed square in Figure 7A, partially on and partly off the top left contact pad. The maps are shown in Figure 7D–F for emission energy, intensity, and charge lifetime, and the dashed black rectangle indicates the approximate region that is on the contact pad. The MHP emission (Figure 7D) in this area is energetically blue shifted by 10–15 meV compared to the rest of the film outside the metal pad. The FWHM of the same region (Figure S8, Supporting Information) is 15 meV larger than the MHP outside the pixel. As expected, the PL intensity in Figure 7E is lowest in the degraded region, and the average recombination lifetime is also significantly lower under the degraded contact region (Figure 7F). This spatial analysis of the flight sample supports the microscopic data from Figure 6, both spectrally and temporally. MHP films behind damaged contacts are consistently found with greater energy, lower PL intensity, and shorter lifetimes than MHP between pixel regions.

3.5. 3cat PSCs with Al Contacts

Figure 8A is an optical image of a 3cat flight sample. Focusing on the left bottom pad in Figure 8B, we see the Al pad is mostly intact, but with several yellow, damaged sections.^[33,34] Figure 8C magnifies the bottom left corner of the pad in Figure 8B and examines the spatial emission profile of the MHP layer using a confocal microscope. The red region along the left edge of the image is uniform emission from the MHP, which is outside the contact area. This area of perovskite is representative of the MHP layer between the contacts. The non-emissive black regions of Figure 8C are those of intact Al. Since the Al is above the absorber layer, as imaged from the front, it blocks incoming excitation and outgoing PL from the MHP. The yellow regions of Figure 8B map one-to-one with the red regions of Figure 8C, verifying that the Al has degraded, revealing the MHP layer beneath. Figure 8D complements this emission with a transmission optical microscopy image of the same area. Here, rather than the false-colored red band of fluorescence microscopy, visible regions of the sample are directly observed with white light passing through the sample. Most of the red emissive regions in Figure 8C also appear dark red in Figure 8D. This deep-red color is due to absorp-

tion in the MHP layer and lies between the black and yellow/grey regions of Figure 8D. In this image, black regions are areas of intact Al, which block the light from below. Black regions of Figure 8C, however, include both the black and yellow/grey regions of Figure 8D. Thus, emissive areas within the Al pixels are found in regions between the intact and degraded metal.

4. Conclusion

Despite contact failure due to Ag and Al degradation, all MISSE-15 hybrid MHP samples remained emissive between contacts after seven months on Earth and eight months in LEO except for the CsPbI₂Br samples. Inorganic perovskite solar cells are typically known to exhibit greater stability than hybrid solar cells when stressed by prolonged heat or moisture.^[35] That stability did not extend to long-duration exposure to environmental stressors in LEO. Further investigation is needed to identify the degradation mechanisms for the CsPbI₂Br material in LEO. Like the flight samples of MISSE-13^[15] and 16, the hybrid MHP devices herein showed no signs of damage from proton irradiation, UV exposure, or the increased AM0 light intensity. We performed microscopy and spectroscopy to investigate damaged Ag and Al contacts, as well as the MHP layer behind each metal contact. While the exact cause of metal migration is not understood and work is ongoing, both Ag and Al were found to penetrate the cell stack and damage the MHP layer. Ag pixels across all flight samples yellowed from the edge inward, degrading more extensively and uniformly than the Al contacts. The Al pixels of triple cation flight samples feature smaller, more isolated yellow regions. This damage is less uniform, as some pixels appear almost unchanged while others are mostly yellow. All five control samples contained Ag feature pixel damage, though far less severe than the flight samples. The two control samples with Al contacts show no signs of decay or migration. Ultimately, microscopic and spectroscopic data revealed partially damaged MHP behind yellow contacts. Perovskites were energetically blue-shifted and exhibited shorter lifetimes in these areas. This damage was highly localized, as these PL metrics returned to values like those in the undamaged regions within 100 μm of the yellowed contacts. These results have already informed researchers who are planning future experiments in space.^[36,37] MISSE-19, currently underway, is utilizing new MHP device architectures without Ag or Al top contacts to avoid ion migration.^[38]

5. Experimental Section

Sample Synthesis: For the MAPI samples, the perovskite precursor solution (ink) was synthesized by mixing 159 mg methylammonium iodide (MAI, GreatCell Solar) and 461 mg PbI_2 (TCI Chemicals) in 17 μL 1-Methyl-2-pyrrolidone (NMP, Sigma–Aldrich), 58 μL Dimethyl sulfoxide (DMSO, Sigma–Aldrich), and 758 μL Dimethylformamide (DMF, Sigma–Aldrich). The p–n MAPI devices were fabricated using 1×3 in. ITO-patterned borosilicate substrates from Colorado Concept Coatings. These substrates were cleaned by sonicating for 10 min each in deionized water, acetone, and isopropyl alcohol, then dried with a N_2 gun. The samples were exposed to 15 min of UV ozone immediately prior to deposition of the HTL. The Poly(triaryl amine), Poly[bis(4-phenyl)(2,4,6-trimethylphenyl)amine] (PTAA, Sigma–Aldrich) HTL (8 mg mL^{-1} in toluene from Sigma–Aldrich) was blade-coated and annealed at 100 °C for 10 min. Poly(9,9-bis(3'-(N,N-dimethyl)-N-ethylammoniumpropyl-2,7-fluorene)-alt-2,7-(9,9-dioctylfluorene))dibromide (PFN-Br from 1-Material) (0.4 mg mL^{-1} in methanol from Sigma–Aldrich) was then blade-coated to improve interfacial compatibility between the PTAA and perovskite layers. The MAPI solution was blade-coated and nitrogen quenched with an air knife and then annealed at 140 °C for 2 min on a hot plate. Blade coating was conducted in ambient conditions, with a gap of 100 μm to the substrate. The subsequent layers were deposited via thermal evaporation: 20 nm Buckminsterfullerene (C_{60} , Luminescence Technology Corp.), 6 nm Bathocuproine (BCP, TCI Chemicals), and 100 nm of Ag (Kurt J. Lesker).

For the F-3cat samples, two perovskite precursor solutions were prepared inside a nitrogen-filled glovebox. For the FACs PbI_3 solution, 224 mg of formamidinium iodide (FAI, GreatCell Solar), 16.9 mg of cesium iodide (CsI, Sigma–Aldrich), 10 mg of methylammonium chloride (MACl, GreatCell Solar), and 666 mg of lead(II) iodide (PbI_2 , TCI Chemicals) were dissolved in 1 mL of a mixed solvent containing DMF and DMSO (850:150 v/v). For the MAPb Br_3 solution, 146 mg of methylammonium bromide (MABr, GreatCell) and 477 mg of lead(II) bromide (PbBr_2 , Sigma–Aldrich, 5×9) were dissolved in 1 mL of the same DMF/DMSO (850:150 v/v) solvent mixture. Both solutions were vortex-shaken for 120 min at room temperature until completely dissolved and then filtered through a 0.45 μm PTFE filter prior to use. The FACs PbI_3 and MAPb Br_3 precursor solutions were then mixed in a 95:5 v/v ratio to form the final perovskite precursor solution. The perovskite layer was deposited using a two-step spin-coating process. First, the precursor solution was deposited onto the substrate and spin-coated at 1000 rpm with an acceleration of 1000 rpm s^{-1} for 10 s, immediately followed by a second step at 6000 rpm with an acceleration of 2000 rpm s^{-1} for 20 s. During the second spin-coating step, 150 μL of chlorobenzene (anti-solvent) was rapidly dispensed onto the center of the spinning substrate 5 s before the end of the program. The formation of the perovskite phase was indicated by an immediate color change. The films were then annealed on a hotplate at 100 °C for 30 min inside the glovebox to complete the crystallization process.

For the triple-cation samples, the perovskite precursor solution was fabricated by mixing 507 mg lead iodide (PbI_2 , TCI Chemicals), 73.4 mg lead bromide (PbBr_2 , TCI Chemicals), 22.4 mg methylammonium bromide (MABr2, GreatCell Solar), 172 mg formamidinium iodide (FAI, GreatCell Solar), and 15.6 mg cesium iodide (CsI, Sigma–Aldrich) in 1 mL of a DMF/DMSO solvent mixture (4:1 v/v) and vortexed to form a 1.26 M ink. The ink was filtered using a 0.45 μm nylon filter. For device fabrication, 25 mm × 25 mm ITO-patterned borosilicate substrates (from Colorado Concept Coatings) were cleaned by sonicating for 10 min each in deionized water, acetone, and isopropyl alcohol, then dried with a N_2 gun. The samples were exposed to 10 min of UV ozone immediately prior to deposition of the ETL. For the ETL, Tin (IV) oxide nanoparticles (Alfa Aesar) were mixed in water (4:1 v/v) and vortexed, then filtered with a 0.45 μm filter. 150 μL of SnO_2 colloid solution was dispensed on the substrate, then spin-coated at 3000 rpm for 15 s, and then annealed at 150 °C for 30 min. The samples were then UV-ozone cleaned again for 10 min, prior to depositing the triple cation perovskite solution in a N_2 glovebox. The perovskite ink (50 μL) was dispensed and spun at 1,000 r.p.m. for 10 s, followed by 6,000 r.p.m. for 20 s. Chlorobenzene (150 μL) was dropped in a continuous

stream onto the spinning substrates with 5 s remaining at the end of the spin cycle. After completion of the spin cycle, the substrate was immediately placed on a hotplate set at 100 °C for 60 min. For the HTL, the PTAA solution was prepared by mixing 10.6 mg PTAA (Solar Chem), 7.5 μL Li-TFSI solution (520 mg in 1 mL acetonitrile, both from Sigma–Aldrich), and 4 μL tert-butylpyridine (tBP, Sigma–Aldrich) in 1 mL toluene. The solution was then filtered using a 0.20 μm syringe filter, and 10 μL was dynamically spin-coated on the perovskite-coated substrates in a N_2 glove box at 5000 r.p.m. for 30 s. After the PTAA layer, 15 nm of molybdenum oxide (MoO_3 , Sigma–Aldrich) and 100 nm of Aluminum (Kurt J. Lesker) were deposited via thermal evaporation.

For the Cs PbI_2Br (all inorganic) cells, the same ETL, HTL, and contact layers were used as those described above for the triple cation samples. For the perovskite ink fabrication, 277 mg PbI_2 (TCI Chemicals), 220 mg PbBr_2 (TCI Chemicals), and 312 mg CsI (Sigma–Aldrich) were mixed in 1 mL of DMSO (Sigma–Aldrich) and vortexed at 60 °C for \approx 1 h to form a 1.2 M ink. The ink was filtered using a 0.45 μm nylon filter. 50 μL of the ink was dropped on the substrate and spun at 1,500 RPM for 15 s, followed by 4,500 r.p.m. for 45 s. 150 μL Methyl acetate was dropped in a continuous stream onto the spinning substrates with 15 s remaining at the end of the spin cycle. After completion of the spin cycle, the substrate was immediately placed on a hotplate set at 135 °C for 1 min.

Confocal Microscopy: Fluorescence confocal microscopy images were acquired with an LSM 880 confocal microscopy system, where a 405 nm laser was used to excite the samples, and emitted light was collected between 750 and 800 nm.

Photoluminescence (PL) Spectroscopy: Samples were illuminated with a pulsed 532 nm laser (NKT Photonics SuperK with an acousto-optic modulator), operating at a repetition rate of 39 MHz and directed through an optical objective. Emitted light was passed through a 650 nm long-pass filter before being detected by a spectrometer (Princeton Instruments Acton 2300) and a single-photon avalanche diode (PicoQuant PDM series). A 500 nm blaze grating with 300 lines mm^{-1} was used to disperse the light onto a CCD detector.

PL Mapping: Photoluminescence maps were generated using a 100× Nikon objective. Samples were scanned using Newport 300 translation stages controlled by a custom LabVIEW program.

Supporting Information

Supporting Information is available from the Wiley Online Library or from the author.

Acknowledgements

The authors thank Severin Habisreutinger for the fabrication of the FA-rich triple cation devices. This work was supported by funding from the NASA Space Technology Mission Directorate 2019 Early Career Initiative. This work was supported in part by funding from the National Science Foundation award DGE-2125510. This work was authored in part by the National Renewable Energy Laboratory, operated by Alliance for Sustainable Energy, LLC, for the U.S. Department of Energy (DOE) under Contract No. DE-AC36-08GO28308. The NREL authors were supported through an interagency agreement with NASA. The views expressed in the article do not necessarily represent the views of the DOE or the U.S. Government.

Conflict of Interest

The authors declare no conflict of interest.

Data Availability Statement

The data that support the findings of this study are available from the corresponding author upon reasonable request.

Keywords

AM0, ion migration, low Earth orbit, perovskite solar cell, recombination

Received: August 29, 2025

Published online:

- [1] R. Verduci, V. Romano, G. Brunetti, N. Yaghoobi Nia, A. Di Carlo, G. D'Angelo, C. Ciminelli, *Adv. Energy Mater.* **2022**, *12*, 2200125.
- [2] V. Romano, A. Agresti, R. Verduci, G. D'Angelo, *ACS Energy Lett.* **2022**, *7*, 2490.
- [3] J. Yang, Q. Bao, L. Shen, L. Ding, *Nano Energy* **2020**, *76*, 105019.
- [4] T. S. Krause, K. T. VanSant, A. Lininger, K. Crowley, T. J. Peshek, L. McMillon-Brown, *Sol. RRL* **2023**, *7*, 2300468.
- [5] Y. Tu, J. Wu, G. Xu, X. Yang, R. Cai, Q. Gong, *Adv. Mater.* **2021**, *33*, 2006545.
- [6] D. Angmo, S. Yan, D. Liang, A. D. Scully, A. S. R. Chesman, M. Kellam, N. W. Duffy, N. Carter, R. Chantler, C. Chen, M. Gao, *ACS Appl. Energy Mater.* **2024**, *7*, 1777.
- [7] A. R. Kirmani, T. A. Byers, Z. Ni, K. VanSant, D. K. Saini, R. Scheidt, X. Zheng, T. B. Kum, I. R. Sellers, L. McMillon-Brown, J. Huang, B. Rout, J. M. Luther, *Nat. Commun.* **2024**, *15*, 696.
- [8] L. McMillon-Brown, J. M. Luther, T. J. Peshek, *ACS Energy Lett.* **2022**, *7*, 1040.
- [9] G. W. Kim, A. Petrozza, *Adv. Energy Mater.* **2020**, *10*, 2001959.
- [10] A. R. Kirmani, B. K. Durant, J. Grandidier, N. M. Haegel, M. D. Kelzenberg, Y. M. Lao, M. D. McGehee, L. McMillon-Brown, D. P. Ostrowski, T. J. Peshek, B. Rout, I. R. Sellers, M. Steger, D. Walker, D. M. Wilt, K. T. VanSant, J. M. Luther, *Joule* **2022**, *6*, 1015.
- [11] C. Costa, M. Manceau, S. Duzellier, T. Nuns, R. Cariou, *Sol. Energy Mater. Sol. Cells* **2023**, *257*, 112388.
- [12] B. K. Durant, H. Afshari, S. Sourabh, V. Yeddu, M. T. Bamidele, S. Singh, B. Rout, G. E. Eperon, D. Y. Kim, I. R. Sellers, *Sol. Energy Mater. Sol. Cells* **2021**, *230*, 111232.
- [13] F. Lang, G. E. Eperon, K. Frohna, E. M. Tennyson, A. Al-Ashouri, G. Kourkafas, J. Bundesmann, A. Denker, K. G. West, L. C. Hirst, H.-C. Neitzert, S. D. Stranks, *Adv. Energy Mater.* **2021**, *11*, 2102246.
- [14] L. K. Reb, M. Böhmer, B. Predeschly, S. Grott, C. L. Weindl, G. I. Ivandekic, R. Guo, C. Dreißigacker, R. Gernhäuser, A. Meyer, P. Müller-Buschbaum, *Joule* **2020**, *4*, 1880.
- [15] W. Delmas, S. Erickson, J. Arteaga, M. Woodall, M. Scheibner, T. S. Krause, K. Crowley, K. T. VanSant, J. M. Luther, J. N. Williams, J. McNatt, T. J. Peshek, L. McMillon-Brown, S. Ghosh, *Adv. Energy Mater.* **2023**, *13*, 2203920.
- [16] I. Cardinaletti, T. Vangerven, S. Nagels, R. Cornelissen, D. Schreurs, J. Hruby, J. Vodnik, D. Devisscher, J. Kesters, J. D'Haen, A. Franquet, V. Spampinato, T. Conard, W. Maes, W. Deferme, J. V. Manca, *Sol. Energy Mater. Sol. Cells* **2018**, *182*, 121.
- [17] J. He, T. Li, X. Liu, H. Su, Z. Ku, J. Zhong, F. Huang, Y. Peng, Y. Cheng, *Sol. Energy* **2019**, *188*, 312.
- [18] Z. Ouyang, M. Yang, J. B. Whitaker, D. Li, M. F. van Hest, *ACS Appl. Energy Mater.* **2020**, *3*, 3714.
- [19] V. S. Chirvony, K. S. Sekerbayev, D. Pérez-del-Rey, J. P. Martínez-Pastor, F. Palazon, P. P. Boix, T. I. Taurbayev, M. Sessolo, H. J. Bolink, *J. Phys. Chem. Lett.* **2019**, *10*, 5167.
- [20] R. Chuliá-Jordán, E. J. Juárez-Pérez, *J. Phys. Chem. C* **2022**, *126*, 3466.
- [21] A. Sridharan, N. K. Noel, H. Hwang, S. Hafezian, B. P. Rand, S. Kéna-Cohen, *Phys. Rev. Mater.* **2019**, *3*, 125403.
- [22] J. Hieulle, A. Krishna, A. Boziki, J. N. Audinot, M. U. Farooq, J. F. Machado, M. Mladenović, H. Phirke, A. Singh, T. Wirtz, A. Tkatchenko, *Energy Environ. Sci.* **2024**, *17*, 284.
- [23] P.-C. Huang, T.-J. Yang, C.-J. Lin, M.-Y. Wang, W.-C. Lin, *Langmuir* **2024**, *40*, 11873.
- [24] Z. Wang, Z. Zhang, L. Xie, S. Wang, C. Yang, C. Fang, F. Hao, *Adv. Optical Mater.* **2022**, *10*, 2101822.
- [25] F. Zu, C. M. Wolff, M. Ralairisosa, P. Amsalem, D. Neher, N. Koch, *ACS Appl. Mater. Interfaces* **2019**, *11*, 21578.
- [26] S. Kim, H. V. Quy, H. W. Choi, C. W. Bark, *Energies* **2020**, *13*, 1069.
- [27] F. A. Roghabadi, N. M. R. Fumani, M. Alidaei, V. Ahmadi, S. M. Sadrameli, *Sci. Rep.* **2019**, *9*, 9448.
- [28] S.-W. Lee, S. Kim, S. Bae, K. Cho, T. Chung, L. E. Mundt, S. Lee, S. Park, H. Park, M. C. Schubert, S. W. Glunz, Y. Ko, Y. Jun, Y. Kang, H.-S. Lee, D. Kim, *Sci. Rep.* **2016**, *6*, 38150.
- [29] M. Saliba, T. Matsui, J. Seo, K. Domanski, J. Correa-Baena, M. Nazeeruddin, S. Zakeeruddin, W. Tress, A. Abate, A. Hagfeldt, M. Grätzel, *Energy Environ. Sci.* **2016**, *9*, 1989.
- [30] S. Svanström, T. J. Jacobsson, G. Boschloo, E. M. J. Johansson, H. Rensmo, U. B. Cappel, *ACS Appl. Mater. Interfaces* **2020**, *12*, 7212.
- [31] K. Kranthiraja, M. Parashar, R. K. Mehta, S. Aryal, M. Tamsal, A. B. Kaul, *Sci. Rep.* **2022**, *12*, 18574.
- [32] J. Li, Q. Dong, N. Li, L. Wang, *Adv. Energy Mater.* **2017**, *7*, 1602922.
- [33] A. Guerrero, J. You, C. Aranda, Y. S. Kang, G. Garcia-Belmonte, H. Zhou, J. Bisquert, Y. Yang, *ACS Nano* **2016**, *10*, 218.
- [34] H. Ding, B. Li, S. Zareen, G. Li, Yi Tu, D. Zhang, Xu Cao, Q. Xu, S. Yang, S. L. Tait, J. Zhu, *ACS Appl. Mater. Interfaces* **2020**, *12*, 28861.
- [35] Q. Zeng, X. Zhang, C. Liu, T. Feng, Z. Chen, W. Zhang, W. Zheng, H. Zhang, B. Yang, *Sol. RRL* **2019**, *3*, 1800239.
- [36] A. R. Kirmani, D. P. Ostrowski, K. T. VanSant, T. A. Byers, R. C. Bramante, K. N. Heinselman, J. Tong, B. Stevens, W. Nemeth, K. Zhu, I. R. Sellers, B. Rout, J. M. Luther, *Nat. Energy* **2023**, *8*, 191.
- [37] S. S. Zhang, Z. H. Liu, W. J. Zhang, Z. Y. Jiang, W. T. Chen, R. Chen, Y. Q. Huang, Z. C. Yang, Y. Q. Zhang, L. Y. Han, W. Chen, *Adv. Energy Mater.* **2020**, *10*, 2001610.
- [38] K. T. VanSant, A. R. Kirmani, J. B. Patel, L. E. Crowe, D. P. Ostrowski, B. M. Wieliczka, M. D. McGehee, L. T. Schelhas, J. M. Luther, T. J. Peshek, L. McMillon-Brown, *ACS Appl. Energy Mater.* **2023**, *6*, 10319.